Anomalous hydrodynamics in a class of scarred frustration-free Hamiltonians

Jonas Richter[*] and Arijeet Pal

Department of Physics and Astronomy, University College London, Gower Street, London WC1E 6BT, UK

(Dated: April 1, 2025)

Atypical eigenstates in the form of quantum scars and fragmentation of Hilbert space due to conservation laws provide obstructions to thermalization in the absence of disorder. In certain models with dipole and $U(1)$ conservation, the fragmentation results in subdiffusive transport. In this paper we study the interplay between scarring and weak fragmentation giving rise to anomalous hydrodynamics in a class of one-dimensional spin-1 frustration-free projector Hamiltonians, known as deformed Motzkin chain. The ground states and low-lying excitations of these chains exhibit large entanglement and critical slowdown. We show that at high energies the particular form of the projectors causes the emergence of disjoint Krylov subspaces for open boundary conditions, with an exact quantum scar being embedded in each subspace, leading to slow growth of entanglement and localized dynamics for specific out-of-equilibrium initial states. Furthermore, focusing on infinite temperature, we unveil that spin transport is subdiffusive, which we corroborate by simulations of suitable stochastic cellular automaton circuits. Compared to dipole moment conserving systems, the deformed Motzkin chain appears to belong to a different universality class with distinct dynamical transport exponent and only polynomially many Krylov subspaces.

Introduction.– Unraveling the intricate dynamics of isolated many-body quantum systems has attracted a vast amount of interest in recent years [1–5]. In this context, transport processes represent arguably one of the most generic nonequilibrium situations and the common expectation is that hydrodynamics emerges naturally from the underlying unitary time evolution [6, 7]. The emergence of a variety of universal hydrodynamics and their relevance to transport coefficients are actively pursued theoretically with potential for utility in near-term quantum devices [6–9]. Enormous experimental efforts have been undertaken to study quantum transport in various platforms, including mesoscopic and solid-state settings as well as cold-atom quantum simulators (see e.g., [10–14]), remarkably allowing to observe even anomalous types of hydrodynamics [15, 16].

While most quantum systems relax to thermal equilibrium, as explained by the eigenstate thermalization hypothesis (ETH) [17–19] and numerically confirmed for a variety of models (e.g., [3, 20–28]), several counterexamples to this paradigm have been identified, with integrable and many-body localized systems being prime examples [29–31]. Moreover, studies of the so-called PXP model revealed that also weaker violations of the ETH are possible, where rare nonthermal states coexist with thermal eigenstates at the same energy density [32, 33], now usually referred to as quantum many-body scars [33–39]. By now, quantum scars have been found in various models [33–52], and tailored embedding procedures further allow to place nonthermal eigenstates into the spectrum of chaotic many-body Hamiltonians [53, 54].

Building on insights from fractonic systems [55–57], the phenomenon of Hilbert-space fragmentation provides yet another mechanism to break ergodicity [58–61]. Hilbert-space fragmentation occurs, for instance, in locally interacting models which in addition to a $U(1)$ charge also conserve the associated dipole moment, though other possibilities have been discussed as well [62–66]. In such cases, the Hilbert space splits into exponentially many disconnected blocks, often referred to as Krylov subspaces, despite states in different subspaces having the same symmetries. While some subspaces might be integrable or localized, others can be chaotic [61, 63, 67]. Even within the thermalizing regimes of such models, the constraints on excitations, e.g., higher-order conservation laws, have implications on the dynamics and lead to subdiffusive transport [68–73], reminiscent of disordered models close to the many-body localization transition [74–76]. The class of frustration-free Hamiltonians considered in this Letter similarly exhibits disjoint Krylov subspaces and subdiffusive hydrodynamics. The underlying mechanisms, however, will be distinct from those of the models mentioned above.

Another motivation for this paper is given by recent work on quantum many-body scars and Hilbert-space fragmentation in Fredkin chains [77]. The Fredkin model is a spin-1/2 chain, where the Hamiltonian is a sum over projectors and can be rewritten in the form of a dressed Heisenberg chain [78], bearing resemblance to other kinetically constrained models [79–81]. While the model is nonintegrable in general, its degenerate ground-state manifold is known analytically [78]. In particular, as shown in [77], the degenerate states can be moved to the center of the spectrum by generalizing the model [82, 83], with each state belonging to a different Krylov subspace.

Here, we consider a closely related class of models, known as deformed Motzkin chain [84–90]. While the ground-state properties of Motzkin chains have been explored in a series of works [84–93], much less is known about the nature of thermalization and nonequilibrium dynamics. In this work, we show that the particular form of the Hamiltonian leads to an intriguing interplay of disconnected Krylov subspaces and exact quantum many-body scars, similar to [77]. As a main result, we unveil
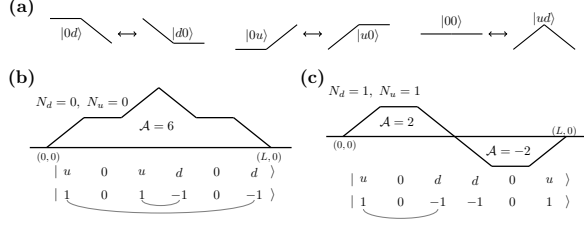
FIG. 1. Identification of $|1\rangle$, $|-1\rangle$, $|0\rangle$ as $|u\rangle$, $|d\rangle$, $|0\rangle$, corresponding to *up*, *down*, and *horizontal* moves on a plane. **(a)** Local updates induced by the projectors of $\mathcal{H}_\nu$. **[(b),(c)]** For OBC, the Hilbert space splits into Krylov subspaces labeled by N_d and N_u. Panel (b) shows example configuration with $N_d = N_u = 0$. Paired spins are indicated by arcs. Panel (c) shows a configuration with $N_d = N_u = 1$. The area $\mathcal{A}$ determines the weight of the basis state within $|S_\nu\rangle$, see Eq. (3).

that the Motzkin chain exhibits subdiffusive hydrodynamics at infinite temperature, which we corroborate by simulations of suitable stochastic cellular automaton circuits [68–70, 94, 95]. Furthermore, we demonstrate that the scarred eigenstates lead to localized dynamics for specific out-of-equilibrium states and parameter regimes.

The model.– We consider a class of spin-1 projector Hamiltonians, $\mathcal{H}_\nu = \sum_\ell \Pi_{\ell,\ell+1}(\nu)$, known as deformed Motzkin chain [84–93],

$$\Pi_{\ell,\ell+1}(\nu) = c_1\,|D_\nu\rangle\langle D_\nu| + c_2\,|U_\nu\rangle\langle U_\nu| + c_3\,|V_\nu\rangle\langle V_\nu| \ , \quad (1)$$

where c_1, c_2 and c_3 are real-valued coefficients, $\nu \geq 0$ is a deformation parameter, and the terms $|\cdot\rangle\langle\cdot|$ are given by $|D\rangle = (|0d\rangle - \nu\,|d0\rangle)/\sqrt{1+\nu^2}$, $|U\rangle = (|u0\rangle - \nu\,|0u\rangle)/\sqrt{1+\nu^2}$, $|V\rangle = (|ud\rangle - \nu\,|00\rangle)/\sqrt{1+\nu^2}$ and should be understood as acting on two neighboring sites ℓ and $\ell+1$. We adopt the convention to denote the three eigenstates of a local spin-1 operator S_ℓ^z as $|u\rangle \equiv |+1\rangle$, $|d\rangle \equiv |-1\rangle$ and $|0\rangle$, where $|u\rangle$ ("*up*"), $|d\rangle$ ("*down*"), and $|0\rangle$ are interpreted as the moves $(x,y) \rightarrow (x+1, y+1)$, $(x,y) \rightarrow (x-1, y-1)$, and $(x,y) \rightarrow (x+1, y)$ on a two-dimensional plane [86], see Fig. 1. The terms $|\cdot\rangle\langle\cdot|$ in Eq. (1) have eigenvalues 0 and 1 such that $\mathcal{H}_\nu$ has a positive-semidefinite spectrum if all $c_i \geq 0$. $\mathcal{H}_\nu$ has a $U(1)$ symmetry, such that $S^z = \sum_\ell S_\ell^z$ is conserved. Written in terms of usual spin-1 operators, $\mathcal{H}_\nu$ takes on a bilinear-biquadratic form [88, 91, 92].

For a spin configuration on L sites, the identification of spins as moves leads to a "random walk". In the $S^z = 0$ sector, these walks start at $(0,0)$ and end at $(L,0)$, see Figs. 1 (b) and (c). For open boundary conditions (OBC), an important concept is then the distinction between *paired* and *unpaired* moves [84]. An up move is called unpaired if there is no matching down move further to the right in the chain, and a down move is unpaired if there is no matching up move further to the left. Given a configuration with no unpaired moves, the height profile never crosses the horizon [Fig. 1 (b)]. Such walks in the
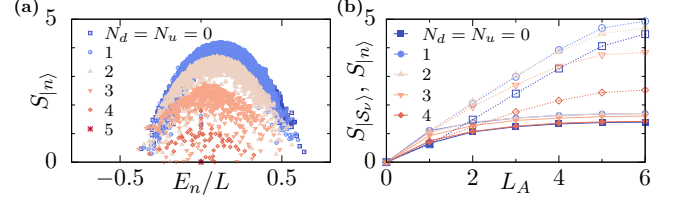

FIG. 2. **(a)** Eigenstate entanglement $S_{|n\rangle}$ for OBC, $L = 10$, and $\nu = 1$, labeled according to their Krylov subspace. **(b)** $S_{|\mathcal{S}_\nu\rangle}$ (filled, solid) at $\nu = 1$ versus subsystem size L_A for $L = 12$ and different $\mathcal{K}_{du}$ with $N_d = N_u$. As a comparison, the entanglement $S_{|n\rangle}$ (open, dashed) of an eigenstate directly adjacent to $|\mathcal{S}_\nu\rangle$ is shown. We have $c_1 = c_3 = 1$, and $c_2 = -1$.

upper half-plane are referred to as Motzkin paths, giving rise to the name of the model.

Disconnected Krylov subspaces.– In the case of OBC, the Hilbert space of $\mathcal{H}_\nu$ splits into Krylov subspaces due to the interplay of the boundary conditions and the action of the projectors on neighboring spins, cf. Fig. 1 (a). The subspaces can be understood as equivalence classes, where each spin configuration is equivalent to a specific root state $|\psi_{du}\rangle$ [84]. Given an arbitrary configuration, $|\psi_{du}\rangle$ can be defined as follows. First, identify *pairs* of up and down spins, where the spins forming a pair do not have to be nearest neighbors, cf. Figs. 1 (b) and (c). Secondly, flip both spins to the $|0\rangle$ state and move the zeros to the center, which eventually yields [84],

$$|\psi_{du}\rangle = |\underbrace{dd\cdots dd}_{N_d}\,\underbrace{00\cdots 00}_{L-N_d-N_u}\,\underbrace{uu\cdots uu}_{N_u}\rangle \ , \quad (2)$$

where N_d and N_u denote the numbers of unpaired down or up moves. Given $|\psi_{du}\rangle$, its corresponding Krylov subspace $\mathcal{K}_{du} = \mathcal{K}(\mathcal{H}_\nu, |\psi_{du}\rangle)$ follows as $\mathcal{K}_{du} = \mathrm{span}\{|\psi_{du}\rangle, \mathcal{H}_\nu\,|\psi_{du}\rangle, \mathcal{H}_\nu^2\,|\psi_{du}\rangle, \dots\}$. In particular, two spin configurations which correspond to different $|\psi_{du}\rangle$ cannot be transformed into each other by the action of $\mathcal{H}_\nu$. As an example, consider $|\psi_1\rangle = |u\cdots ud\cdots d\rangle$ and $|\psi_2\rangle = |d\cdots du\cdots u\rangle$, which both have $S^z = 0$. However, while $|\psi_1\rangle$ belongs to $\mathcal{K}_{00}$ (i.e., it is equivalent to $|0\cdots 0\rangle$), $|\psi_2\rangle$ belongs to $\mathcal{K}_{L/2 L/2}$. In fact, $|\psi_2\rangle$ is an exact eigenstate of $\mathcal{H}_\nu$, i.e., it spans a subspace of dimension one. Apparently the degree of "Hilbert-space fragmentation" in the Motzkin chain is weaker compared to, e.g., models with charge and dipole conservation, which exhibit exponentially many subspaces [58–60]. For instance, in the $S^z = 0$ sector, there are only $L/2 + 1$ separate $\mathcal{K}_{du}$ labeled by $0 \leq N_d = N_u \leq L/2$, i.e., the total number of subspaces grows only polynomially with L. An expression for the dimension $\mathcal{D}_{du}$ of each $\mathcal{K}_{du}$ can be derived combinatorially [96]. In particular, for $\mathcal{K}_{du}$ with small $N_d + N_u$, $\mathcal{D}_{du}$ is expected to grow exponentially with L. At the same time, for any finite L, there always exist $\mathcal{K}_{du}$ with $\mathcal{D}_{du} = 1$ (namely when $N_d + N_u = L$), as well as small subspaces with $\mathcal{D}_{du} \propto L$.

For subspaces with large $\mathcal{D}_{du}$, thermalization is expected to occur. This is visualized in Fig. 2 (a) in terms of the eigenstate entanglement entropy $S_{|n\rangle} = -\text{Tr}[\rho_A \ln \rho_A]$, where $\rho_A = \text{Tr}_B\{|n\rangle\langle n|\}$ is the reduced density matrix for a half-chain bipartition. While the overall distribution of $S_{|n\rangle}$ is rather broad, it looks thermal when focusing on individual $\mathcal{K}_{du}$ with small N_d, N_u. At the same time, the low values of $S_{|n\rangle}$ in the center of the spectrum mostly belong to $\mathcal{K}_{du}$ with large N_d, N_u, where the maximally achievable entanglement is limited due to small $\mathcal{D}_{du}$. Moreover, as shown in [97], individual $\mathcal{K}_{du}$ indeed exhibit chaotic energy-level statistics and most eigenstates follow the ETH.

Exact quantum many-body scars.– Despite $\mathcal{H}_\nu$ being nonintegrable and chaotic, a number of eigenstates $|\mathcal{S}_\nu\rangle$ can be constructed combinatorially [84–86]. In this context, the key quantity is the area $\mathcal{A}_k$ enclosed by the height profile of a given spin configuration $|k\rangle$, where areas below the horizon contribute negatively, cf. Figs. 1 (b) and (c). Within each $\mathcal{K}_{du}$, $|\mathcal{S}_\nu\rangle$ is then given by the area-weighted superposition [84–86] (see also [97]),

$$|\mathcal{S}_\nu\rangle = \frac{1}{\sqrt{M'_\nu}}\sum_{k=1}^{\mathcal{D}_{du}} \nu^{\mathcal{A}_k}|k\rangle = \frac{1}{\sqrt{M_\nu}}\sum_{k=1}^{\mathcal{D}_{du}} \nu^{-\mathcal{P}_k}|k\rangle , \quad (3)$$

where the sum runs over all $\mathcal{D}_{du}$ basis states $|k\rangle$, $\mathcal{P} = \sum_{\ell=1}^{L}\ell S_\ell^z$ is the dipole operator with $\mathcal{P}_k = \langle k|\mathcal{P}|k\rangle$, and M'_ν and M_ν ensure normalization. The states $|\mathcal{S}_\nu\rangle$ have exactly zero energy as they are annihilated by all projectors in Eq. (1) [84–86]. According to Eq. (3), $|\mathcal{S}_\nu\rangle$ is dominated by $|k\rangle$ with large positive $\mathcal{P}_k$ if $\nu < 1$. In contrast, for $\nu > 1$, $|k\rangle$ with large negative $\mathcal{P}_k$ dominate. At $\nu = 1$, $|\mathcal{S}_\nu\rangle$ is an equal-weight superposition of all states in $\mathcal{K}_{du}$, reminiscent of the Rokhsar-Kivelson ground state in quantum dimer models [104].

By choosing suitable c_i in Eq. (1), the $|\mathcal{S}_\nu\rangle$ can be shifted close to the center of the spectrum [105], where they act as quantum many-body scars due to their subvolume-law entanglement [84–86], similar to other examples of frustration-free ground states being embedded by deforming the underlying model [43–45]. The nonthermal nature of the $|\mathcal{S}_\nu\rangle$ is emphasized in Fig. 2 (b), where $S_{|\mathcal{S}_\nu\rangle}$ is shown versus subsystem size L_A for different $\mathcal{K}_{du}$. In particular, $S_{|\mathcal{S}_\nu\rangle}$ is compared to the entanglement of an eigenstate directly adjacent to $|\mathcal{S}_\nu\rangle$, demonstrating that typical eigenstates are extensively entangled whereas $|\mathcal{S}_\nu\rangle$ is not. As shown in [97], $|\mathcal{S}_\nu\rangle$ also violates the ETH by yielding atypical expectation values for local operators.

While the construction of $\mathcal{K}_{du}$ as in Eq. (2) does not apply to periodic boundary conditions (PBC), we note that quantum scars appear to exist also for PBC [97].

Anomalous hydrodynamics.– We probe the transport properties of $\mathcal{H}_\nu$ in terms of the infinite-temperature correlation function $C(r,t)$,

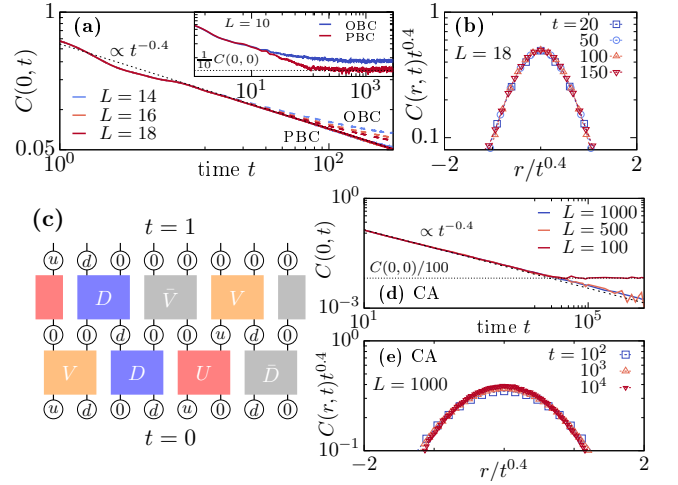$$C(r,t) = \text{Tr}[S_{\ell+r}^z(t)S_\ell^z]/3^L , \quad (4)$$

FIG. 3. **(a)** $C(0,t)$ for PBC (solid) and OBC (dashed) at $\nu = 1$ and $L = 14, 16, 18$. A power law $\propto t^{-1/z}$ with $z = 5/2$ is shown for comparison (dotted). The inset shows data for $L = 10$ up to longer times. **(b)** $C(r,t)t^{0.4}$ versus $r/t^{0.4}$ at fixed times. We have $c_1 = c_3 = 1$ and $c_2 = -1$ in all cases. **(c)** Exemplary time step in the cellular automaton (CA) circuit, consisting of two layers of two-site updates. Given a particular configuration of two sites, one of the updates D, U, or V is chosen, while with probability $1/2$, we instead apply $\bar{D}$, $\bar{U}$, or $\bar{V}$, leaving the spin configuration unchanged (see [97] for more details). **[(d),(e)]** Analogous data as in panels (a) and (b), but now obtained by CA circuits for larger L.

where $S_{\ell+r}^z(t) = e^{i\mathcal{H}t}S_{\ell+r}^z e^{-i\mathcal{H}t}$, and r is the distance between the two sites [106]. In case of diffusion, $C(r,t)$ takes on a Gaussian shape with a standard deviation $\sigma(t) \propto t^{1/z}$ with $z = 2$ [6, 107]. Correspondingly, the autocorrelation function $C(r = 0,t)$ acquires a hydrodynamic tail, $C(0,t) \propto t^{-1/z}$. For a thermalizing system, one expects a uniform distribution at long times, $C(r,t \to \infty) \to C_{\text{eq}}$, where $C_{\text{eq}} = C(0,0)/L$ [6]. We exploit quantum typicality [97, 108, 109] to simulate $C(r,t)$ for spin-1 systems up to $L = 18$, beyond the range of full exact diagonalization. Focusing on $\nu = 1$, we find that $C(0,t) \propto t^{-1/z}$ with $z \approx 5/2$ [Fig. 3 (a)], suggesting that spin transport in the Motzkin chain is not diffusive but subdiffusive instead, both for PBC and OBC. In the latter case, the power law persists on a shorter time scale as $C(0,t)$ saturates to a higher long-time value $C(0,t \to \infty) > C_{\text{eq}}$ [inset of Fig. 3 (a)] due to the disjoint $\mathcal{K}_{du}$. We expect this difference between PBC and OBC to disappear in the thermodynamic limit $L \to \infty$, where the exponentially large $\mathcal{K}_{du}$ dominate. Subdiffusive spin transport is further substantiated in Fig. 3 (b), where the correlations $C(r,t)$ for different t nicely collapse onto each other if the data and r are rescaled with $t^{1/z}$. We note that the observed value of z is distinct from that found in dipole-conserving systems, where $z = 4$ [59, 69].

Intuitively, the occurrence of subdiffusion can be understood by considering the updates of local spin config-
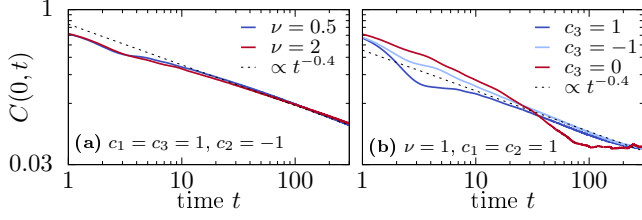
FIG. 4. **(a)** $C(0,t)$ at $\nu = 0.5, 2$ for $c_1 = c_3 = 1$, $c_2 = -1$. A power law $\propto t^{-0.4}$ is shown for comparison. **(b)** $C(0,t)$ at $\nu = 1$ for $c_3 = -1, 0, 1$ and $c_1 = c_2 = 1$. We have $L = 16$ and PBC in all cases.

urations induced by $\mathcal{H}_\nu$, cf. Fig. 1 (a). As there are no matrix elements connecting $|du\rangle \leftrightarrow |00\rangle$ or $|du\rangle \leftrightarrow |ud\rangle$, configurations $|du\rangle$ act as bottlenecks. Particularly, extended regions of the form $|\cdots ddduuu \cdots\rangle$ will slow down the dynamics. This argument can also be stated more formally by inspecting the spin-current operator of $\mathcal{H}_\nu$, see [97]. While we cannot provide a full hydrodynamic theory, we here proceed by constructing a stochastic cellular automaton (CA) circuit, see Fig. 3 (c) and [97], which mimics the terms appearing in $\mathcal{H}_\nu$ and allows to access large systems and long times [68–70, 94, 95]. The so-obtained data for $L \leq 10^3$ and $t \leq 10^6$ in Figs. 3 (d) and (e) corroborate our findings of anomalous hydrodynamics with $z \approx 5/2$ at infinite temperature. Putting these results into perspective, we note that subdiffusive dynamics in Motzkin chains [89, 91, 92] (and related Fredkin models [110]) has been observed before at low temperatures, where a larger $z \approx 3$ was found by analyzing the scaling of low-lying energy gaps. Connecting these low-temperature results to our finding of $z \approx 2.5$ at infinite temperature is an open issue for future work. In this context, we note that our usage of CA circuits was also inspired by the mapping between Rokhsar-Kivelson Hamiltonians and statistical-mechanics models [111, 112], proposed in [91] to explain the origin of subdiffusion.

While we have focused on $\nu = 1$ in Fig. 3, we stress that the occurrence of high-temperature subdiffusion with $z \approx 5/2$ in fact seems robust for a wider range of parameters. This is demonstrated in Fig. 4, where $C(0,t) \propto t^{-0.4}$ both for $\nu = 0.5, 2$, as well as for $\nu = 1$ but different choices of c_i. Only for $c_3 = 0$, the decay of $C(0,t)$ appears to be different, which can be explained by the fact that $\mathcal{H}_\nu$ becomes integrable in this limit [113].

As an aside, we note that the anomalous transport properties of $\mathcal{H}_\nu$ also reflect themselves in an unusual growth of Rényi entropies $S_\alpha(t) = \ln \text{Tr}[\rho_A^\alpha]/(1 - \alpha)$, $\rho_A = \text{Tr}_B |\psi(t)\rangle \langle\psi(t)|$, which were argued to grow sub-ballistically for $\alpha > 1$ [114, 115], see [97] for details.

Initial-state dependence.– While $C(r,t)$ represents a high-temperature average, studying quantum quenches with individual out-of-equilibrium states reveals the impact of the quantum scar $|\mathcal{S}_\nu\rangle$ on the dynamics. In particular, given its construction in Eq. (3), the dynamics
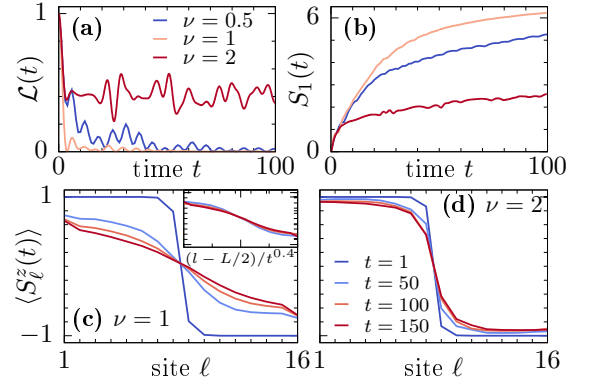

FIG. 5. Dynamics of domain-wall state for $L = 16$ and OBC. **[(a),(b)]** $\mathcal{L}(t) = |\langle\psi(t)|\psi\rangle|^2$ and $S_1(t)$ for $\nu = 0.5, 1, 2$. **[(c),(d)]** $\langle S_\ell^z(t)\rangle$ at fixed t for $\nu = 1, 2$. Inset in (c) shows data at $t = 50, 100, 150$ versus $(\ell - L/2)/t^{0.4}$.

can be tuned between different regimes depending on the deformation parameter ν. We here exemplify this fact by considering a domain wall $|\psi\rangle = |u \ldots ud \ldots d\rangle$, which is a natural initial condition for quench dynamics [116–119]. While $|\psi\rangle$ has zero energy density, $\langle\psi| \mathcal{H}_\nu |\psi\rangle /L \to 0$, such that thermalization is expected, we note that in the picture of random-walks on a plane (Fig. 1), $|\psi\rangle$ maximizes the area $\mathcal{A}$. According to the construction of $|\mathcal{S}_\nu\rangle$ in Eq. (3), $|\psi\rangle$ therefore contributes dominantly to $|\mathcal{S}_\nu\rangle$ if $\nu > 1$ (here $|\langle\psi|\mathcal{S}_\nu\rangle|^2 \approx 0.64$ for $\nu = 2$ and $L = 16$ [120], in contrast to $|\langle\psi|\mathcal{S}_\nu\rangle|^2 = 1/\mathcal{D}_{du}^2$ for $\nu = 1$). As a consequence, we find that $\mathcal{L}(t) = |\langle\psi(t)|\psi\rangle|^2$ decays quickly for $\nu = 0.5, 1$, while $\mathcal{L}(t)$ oscillates around a finite value for $\nu = 2$ [Fig. 5 (a)]. Likewise, the growth of the von Neumann entropy $S_1(t)$ [122] is significantly slower for $\nu = 2$ [Fig. 5 (b)]. As shown in [97], there also exist initial states where dynamics is instead slower for $\nu < 1$ and faster for $\nu > 1$.

By tuning ν and thereby controlling its overlap with $|\mathcal{S}_\nu\rangle$, it is thus possible to obstruct thermalization of $|\psi\rangle$. This is emphasized even more in Figs. 5 (c) and (d), where the spin profiles $\langle S_\ell(t)\rangle = \langle\psi(t)| S_\ell^z |\psi(t)\rangle$ are shown at fixed times for $\nu = 1$ and $\nu = 2$. In particular, for $\nu = 2$, $\langle S_\ell(t)\rangle$ is found to remain localized even at long times. In contrast, for $\nu = 1$, $|\psi\rangle$ is not dominated by $|\mathcal{S}_\nu\rangle$ such that the domain wall melts away, albeit $\langle S_\ell(t)\rangle$ is still rather inhomogeneous even at $t = 150$. In fact, the profiles for different t approximately collapse onto a single curve when plotted against $(l - L/2)/t^{0.4}$ [inset of Fig. 5 (c)], i.e., consistent with the anomalous transport discussed above. We note that similar parameter-dependent melting of domain-wall states is known for other classes of models as well [116, 119].

Conclusion & Outlook.– To summarize, we have studied a class of frustration-free Hamiltonians, where disjoint Krylov subspaces, anomalous hydrodynamics, and exact quantum many-body scars occur simultaneously.

Compared to dipole-conserving or other fractonic models, the Motzkin chain appears to lie in a different "universality class" featuring a distinct dynamical transport exponent $z \approx 5/2$ at infinite temperature and Hilbert-space fragmentation with only polynomially many subspaces. The quantum scars $|\mathcal{S}_\nu\rangle$ are similar to other embeddings of frustration-free ground states by deforming the underlying model [43–45]. Moreover, a similar construction of exact scars in individual Krylov subspaces has been recently presented for related Fredkin chains [77].

Regarding prospective directions of research, we note that while at present an analytical expression is known only for the states $|\mathcal{S}_\nu\rangle$, the data in Fig. 2 suggest that $\mathcal{H}_\nu$ hosts other low-entangled eigenstates beyond $|\mathcal{S}_\nu\rangle$. Approximating further nonthermal eigenstates, e.g., by devising a spectrum generating algebra [123–126] acting on $|\mathcal{S}_\nu\rangle$, might thus be an interesting attempt. Another extension is to study hydrodynamics at finite temperatures to connect our high-temperature results to the subdiffusive scaling of low-energy excitations [91, 92], as well as to consider transport beyond half-filling, where CA circuits have already proven helpful [70]. Finally, the stability of the $|\mathcal{S}_\nu\rangle$ and, particularly, the persistence of anomalous hydrodynamics upon adding different perturbations to $\mathcal{H}_\nu$ is an open question.

∗ j.richter@ucl.ac.uk

[1] A. Polkovnikov, K. Sengupta, A. Silva, and M. Vengalattore, Rev. Mod. Phys. **83**, 863 (2011).

[2] C. Gogolin and J. Eisert, Rep. Prog. Phys. **79**, 056001 (2016).

[3] L. D'Alessio, Y. Kafri, A. Polkovnikov, and M. Rigol, Adv. Phys. **65**, 239 (2016).

[4] F. Borgonovi, F. M. Izrailev, L. F. Santos, and V. G. Zelevinsky, Phys. Rep. **626**, 1 (2016).

[5] T. Mori, T. N. Ikeda, E. Kaminshi, and M. Ueda, J. Phys. B: At. Mol. Opt. Phys. **51**, 112001 (2018).

[6] B. Bertini, F. Heidrich-Meisner, C. Karrasch, T. Prosen, R. Steinigeweg, and M. Žnidarič, Rev. Mod. Phys. **93**, 025003 (2021).

[7] V. Khemani, A. Vishwanath, and D. A. Huse, Phys. Rev. X **8**, 031057 (2018).

[8] B. Ye, F. Machado, C. D. White, R. S. K. Mong, and N. Y. Yao, Phys. Rev. Lett. **125**, 030601 (2020).

[9] J. Richter and A. Pal, Phys. Rev. Lett. **126**, 230501 (2021).

[10] S. Das Sarma, S. Adam, E. H. Hwang, and E. Rossi, Rev. Mod. Phys. **83**, 407 (2011).

[11] C. Hess, Phys. Rep. **811**, 1 (2019).

[12] A. Scheie, N. E. Sherman, M. Dupont, S. E. Nagler, M. B. Stone, G. E. Granroth, J. E. Moore and D. A. Tennant, Nat. Phys. **17**, 726 (2021).

[13] S. Hild, T. Fukuhara, P. Schauß, J. Zeiher, M. Knap, E. Demler, I. Bloch, and C. Gross, Phys. Rev. Lett. **113**, 147205 (2014).

[14] N. Jepsen, J. Amato-Grill, I. Dimitrova, W. W. Ho, E. Demler, and W. Ketterle, Nature **588**, 403 (2020).

[15] D. Wei, A. Rubio-Abadal, B. Ye, F. Machado, J. Kemp, K. Srakaew, S. Hollerith, J. Rui, S. Gopalakrishnan, N. Y. Yao, I. Bloch, and J. Zeiher, arXiv:2107.00038.

[16] M. K. Joshi, F. Kranzl, A. Schuckert, I. Lovas, C. Maier, R. Blatt, M. Knap, and C. F. Roos, arXiv:2107.00033.

[17] J. M. Deutsch, Phys. Rev. A **43**, 2046 (1991).

[18] M. Srednicki, Phys. Rev. E **50**, 888 (1994).

[19] M. Rigol, V. Dunjko, and M. Olshanii, Nature **452**, 854 (2008).

[20] R. Steinigeweg, J. Herbrych, and P. Prelovšek, Phys. Rev. E **87**, 012118 (2013).

[21] W. Beugeling, R. Moessner, and M. Haque, Phys. Rev. E **89**, 042112 (2014).

[22] H. Kim, T. N. Ikeda, D. A. Huse, Phys. Rev. E **90**, 052105 (2014).

[23] E. J. Torres-Herrera and L. F. Santos, Phys. Rev. E **89**, 062110 (2014).

[24] R. Mondaini, K. R. Fratus, M. Srednicki, and M. Rigol, Phys. Rev. E **93**, 032104 (2016).

[25] D. Jansen, J. Stolpp, L. Vidmar, and F. Heidrich-Meisner, Phys. Rev. B **99**, 155130 (2019).

[26] T. LeBlond, K. Mallayya, L. Vidmar, and M. Rigol, Phys. Rev. E **100**, 062134 (2019).

[27] M. Brenes, T. LeBlond, J. Goold, and M. Rigol, Phys. Rev. Lett. **125**, 070605 (2020).

[28] J. Richter, A. Dymarsky, R. Steinigeweg, and J. Gemmer, Phys. Rev. E **102**, 042127 (2020).

[29] F. H. L. Essler and M. Fagotti, J. Stat. Mech. **2016**, 064002 (2016).

[30] R. Nandkishore and D. A. Huse, Annu. Rev. Condens. Matter Phys. **6**, 15 (2015).

[31] D. A. Abanin, E. Altman, I. Bloch, and M. Serbyn, Rev. Mod. Phys. **91**, 021001 (2019).

[32] H. Bernien, S. Schwartz, A. Keesling, H. Levine, A. Omran, H. Pichler, S. Choi, A. S. Zibrov, M. Endres, M. Greiner, V. Vuletić, and M. D. Lukin, Nature **551**, 579 (2017).

[33] C. J. Turner, A. A. Michailidis, D. A. Abanin, M. Serbyn, and Z. Papić, Nat. Phys. **14**, 745 (2018).

[34] S. Moudgalya, S. Rachel, B. A. Bernevig, and N. Regnault, Phys. Rev. B **98**, 235155 (2018).

[35] S. Moudgalya, N. Regnault, and B. A. Bernevig, Phys. Rev. B **98**, 235156 (2018).

[36] V. Khemani, C. R. Laumann, and A. Chandran, Phys. Rev. B **99**, 161101(R) (2019).

[37] S. Choi, C. J. Turner, H. Pichler, W. W. Ho, A. A. Michailidis, Z. Papić, M. Serbyn, M. D. Lukin, and D. A. Abanin, Phys. Rev. Lett. **122**, 220603 (2019).

[38] C.-J. Lin and O. I. Motrunich, Phys. Rev. Lett. **122**, 173401 (2019).

[39] M. Serbyn, D. A. Abanin, and Z. Papić, Nat. Phys. **17**, 675 (2021).

[40] M. Schecter and T. Iadecola, Phys. Rev. Lett. **123**, 147201 (2019).

[41] T. Iadecola and M. Žnidarić, Phys. Rev. Lett. **123**, 036403 (2019).

[42] A. J. A. James, R. M. Konik, and N. J. Robinson, Phys. Rev. Lett. **122**, 130603 (2019).

[43] S. Ok, K. Choo, C. Mudry, C. Castelnovo, C. Chamon,

and T. Neupert, Phys. Rev. Research **1**, 033144 (2019).

[44] J. Wildeboer, A. Seidel, N. S. Srivatsa, A. E. B. Nielsen, and O. Erten, arXiv:2009.00022.

[45] K. Lee, R. Melendrez, A. Pal, and H. J. Changlani, Phys. Rev. B **101**, 241111 (2020).

[46] P. A. McClarty, M. Haque, A. Sen, and J. Richter, Phys. Rev. B **102**, 224303 (2020).

[47] Y. Kuno, T. Mizoguchi, and Y. Hatsugal, Phys. Rev. B **102**, 241115 (2020).

[48] F. M. Surace, P. P. Mazza, G. Giudici, A. Lerose, A. Gambassi, and M. Dalmonte, Phys. Rev. X **10**, 021041 (2020).

[49] H. Zhao, J. Vovrosh, F. Mintert, and J. Knolle, Phys. Rev. Lett. **124**, 160604 (2020).

[50] B. van Voorden, J. Minář, and K. Schoutens, Phys. Rev. B **101**, 220305(R) (2020).

[51] S. Pilatowsky-Cameo, D. Villaseñor, M. A. Bastarrachea-Magnani, S. Lerma-Hernández, L. F. Santos, and J. G. Hirsch, Nat. Commun. **12**, 852 (2021)

[52] J. Jeyaretnam, J. Richter, and A. Pal, Phys. Rev. B **104**, 014424 (2021).

[53] N. Shiraishi and T. Mori, Phys. Rev. Lett. **119**, 030601 (2017).

[54] N. Shiraishi, J. Stat. Mech. **(2019)**, 083103 (2019).

[55] C. Chamon, Phys. Rev. Lett. **94**, 040402 (2005).

[56] M. Pretko, Phys. Rev. B **98**, 115134 (2018).

[57] R. M. Nandkishore and M. Hermele, Annu. Rev. Condens. Matter Phys. **10**, 295 (2019).

[58] S. Pai, M. Pretko, and R. M. Nandkishore, Phys. Rev. X **9**, 021003 (2019).

[59] P. Sala, T. Rakovszky, R. Verresen, M. Knap, and F. Pollmann, Phys. Rev. X **10**, 011047 (2020).

[60] V. Khemani, M. Hermele, and R. Nandkishore, Phys. Rev. B **101**, 174204 (2020).

[61] S. Moudgalya, A. Prem, R. Nandkishore, N. Regnault, and B. A. Bernevig, arXiv:1910.14048.

[62] G. De Tomasi, D. Hetterich, P. Sala, and F. Pollmann, Phys. Rev. B **100**, 214313 (2019).

[63] Z.-C. Yang, F. Liu, A. V. Gorshkov, and T. Iadecola, Phys. Rev. Lett. **124**, 207602 (2020).

[64] W.-H. Li, X. Deng, and L. Santos, arXiv:2103.13780.

[65] K. Lee, A. Pal, and H. J. Changlani, Phys. Rev. B **103**, 235133 (2021).

[66] D. Hahn, P. A. McClarty, and D. J. Luitz, arXiv:2104.00692.

[67] L. Herviou, J. H. Bardarson, and N. Regnault, Phys. Rev. B **103**, 134207 (2021).

[68] J. Iaconis, S. Vijay, and R. Nandkishore, Phys. Rev. B **100**, 214301 (2019).

[69] J. Feldmeier, P. Sala, G. De Tomasi, F. Pollmann, and M. Knap, Phys. Rev. Lett. **125**, 245303 (2020).

[70] A. Morningstar, V. Khemani, and D. A. Huse, Phys. Rev. B **101**, 214205 (2020).

[71] A. Gromov, A. Lucas, and R. M. Nandkishore, Phys. Rev. Research **2**, 033124 (2020).

[72] P. Zhang, Phys. Rev. Research **2**, 033129 (2020).

[73] J. Iaconis, A. Lucas, and R. Nandkishore, Phys. Rev. E **103**, 022142 (2021).

[74] Y. Bar Lev, G. Cohen, and D. R. Reichmann, Phys. Rev. Lett. **114**, 100601 (2015).

[75] K. Agarwal, S. Gopalakrishnan, M. Knap, M. Müller, and E. Demler, Phys. Rev. Lett. **114**, 160401 (2015).

[76] D. J. Luitz and Y. Bar Lev, Ann. Phys. **529**, 1600350 (2017).

[77] C. Langlett and S. Xu, Phys. Rev. B **103**, L220304 (2021).

[78] O. Salberger and V. Korepin, Rev. Math. Phys. **29**, 1750031 (2017).

[79] F. Ritort and P. Sollich, Adv. Phys. **52**, 219 (2003).

[80] Z. Lan, M. van Horssen, S. Powell, and J. P. Garrahan, Phys. Rev. Lett. **121**, 040603 (2018).

[81] N. Pancotti, G. Giudice, J. I. Cirac, J. P. Garrahan, and M. C. Bañuls, Phys. Rev. X **10**, 021051 (2020).

[82] O. Salberger, T. Udagawa, Z. Zhang, H. Katsura, I. Klisch, and V. Korepin, J. Stat. Mech. **(2017)**, 063103 (2017).

[83] K. Adhikari and K. S. D. Beach, Phys. Rev. B **102**, 184415 (2020).

[84] S. Bravyi, L. Caha, R. Movassagh, D. Nagaj, and P. W. Shor, Phys. Rev. Lett. **109**, 207202 (2012).

[85] Z. Zhang, A. Ahmadain, and I. Klich, PNAS **114**, 5142 (2017).

[86] R. Movassagh and P. W. Shor, PNAS **113**, 13278 (2016).

[87] L. Levine and R. Movassagh, J. Phys. A: Math. Theor. **50**, 255302 (2017).

[88] R. Movassagh, J. Math. Phys. **58**, 031901 (2017).

[89] L. Dell'Anna, O. Salberger, L. Babiero, A. Trombettoni, and. V. E. Korepin, Phys. Rev. B **94**, 155140 (2016).

[90] L. Babiero, L. Dell'Anna, A. Trombettoni, V. E. Korepin, Phys. Rev. B **96**, 180404(R) (2017).

[91] X. Chen, E. Fradkin, and W. Witczak-Krempa, J. Phys. A: Math. Theor. **50**, 464002 (2017).

[92] X. Chen, E. Fradkin, and W. Witczak-Krempa, Phys. Rev. B **96**, 180402(R) (2017).

[93] F. Sugino and P. Padmanabhan, J. Stat. Mech. **(2018)**, 013101 (2018).

[94] M. Medenjak, K. Klobas, and T. Prosen, Phys. Rev. Lett. **119**, 110603 (2017).

[95] S. Gopalakrishnan and B. Zakirov, Quantum Sci. Technol. **3**, 033004 (2018).

[96] Generally, the dimension of a Krylov space for a chain of L sites can be derived combinatorially and is given by $\mathcal{D}_{du} = \sum_{i \geq 0}^{2i+N_{du} \leq L} \frac{N_{du}+1}{i+N_{du}+1} \binom{L}{2i+N_{du}} \binom{2i+N_{du}}{i}$, which only depends on the sum $N_{du} = N_d + N_u$ of unpaired up and down spins [84].

[97] See supplemental material for details on Krylov-space restricted thermalization, the construction of $|\mathcal{S}_\nu\rangle$, dynamical quantum typicality, cellular automaton dynamics, additional data on domain-wall melting, entanglement growth, and quench dynamics, as well as the derivation of the spin-current operator, including Refs. [98–103].

[98] V. Oganesyan and D. A. Huse, Phys. Rev. B **75**, 155111 (2007).

[99] H. Liu and S. J. Suh, Phys. Rev. Lett. **112**, 011601 (2014).

[100] C. Chiaracane, F. Pietracaprina, A. Purkayastha, and J. Goold, Phys. Rev. B **103**, 184205 (2021).

[101] H. Fehske, J. Schleede, G. Schubert, G. Wellein, V. S. Filinov and A. R. Bishop, Phys. Lett. A **373**, 2182 (2009).

[102] M. Žnidarič, Commun. Phys. **3**, 100 (2020).

[103] T. Rakovszky, F. Pollmann, and C. von Keyserlingk, Commun. Phys. **4**, 91 (2021).

[104] D. S. Rokhsar and S. A. Kivelson, Phys. Rev. Lett. **61**, 2376 (1988).

[105] With the exception of Fig. 4, we choose $c_1 = c_3 = 1$ and $c_2 = -1$ throughout this work, for which the $|\mathcal{S}_\nu\rangle$ are located close to the center of the spectrum.

[106] Note that the specific site ℓ is irrelevant in the case of PBC, while for OBC, we use $\ell = L/2$.

[107] J. Richter, N. Casper, W. Brenig, and R. Steinigeweg, Phys. Rev. B **100**, 144423 (2019).

[108] F. Jin, D. Willsch, M. Willsch, H. Lagemann, K. Michielsen, and H. De Raedt, J. Phys. Soc. Jpn. **90**, 012001 (2021).

[109] T. Heitmann, J. Richter, D. Schubert, and R. Steinigeweg, Z. Naturforsch. A **75**, 421 (2020).

[110] K. Adhikari and K. S. D. Beach, arXiv:2011.07110.

[111] C. L. Henley, J. Phys.: Condens. Matter **16**, S891 (2004).

[112] C. Castelnovo, C. Chamon, C. Mudry, and P. Pujol, Ann. Phys. **318**, 316 (2005).

[113] B. Tong, O. Salberger, K. Hao, and V. Korepin, arXiv:2009.10368.

[114] T. Rakovszky, F. Pollmann, and C. W. von Keyserlingk, Phys. Rev. Lett. **122**, 250602 (2019).

[115] Y. Huang, IOP SciNotes **1**, 035205 (2020)

[116] D. Gobert, C. Kollath, U. Schollwöck, and G. Schütz, Phys. Rev. E **71**, 036102 (2005).

[117] J. Hauschild, F. Heidrich-Meisner, and F. Pollmann, Phys. Rev. B **94**, 161109 (2016).

[118] M. Ljubotina, M. Žnidarić, and T. Prosen, Nat. Commun. **8**, 16117 (2017).

[119] M. Medenjak and J. De Nardis, Phys. Rev. B **101**, 081411 (2020).

[120] For such cases, with one macroscopically populated eigenstate, a typicality-based framework allows to predict the relaxation of observables based on $\mathcal{L}(t)$ [97, 121].

[121] P. Reimann, B. N. Balz, J. Richter, and R. Steinigeweg, Phys. Rev. B **101**, 094302 (2020).

[122] We refer to the Rényi entropies $S_\alpha(t) = \ln \mathrm{Tr}[\rho_A^\alpha]/(1-\alpha)$ which yield $S_1(t) = -\mathrm{Tr}[\rho_A \ln \rho_A]$ for $\alpha = 1$.

[123] D. K. Mark, C.-J. Lin, and O. I. Motrunich, Phys. Rev. B **101**, 195131 (2020).

[124] S. Moudgalya, N. Regnault, and B. A. Bernevig, Phys. Rev. B **102**, 085140 (2020).

[125] K. Pakrouski, P. N. Pallegar, F. K. Popov, and I. R. Klebanov, Phys. Rev. Lett. **125**, 230602 (2020)

[126] N. O'Dea, F. Burnell, A. Chandran, and V. Khemani, Phys. Rev. Research **2**, 043305 (2020).

SUPPLEMENTAL MATERIAL

Krylov-space restricted thermalization

Periodic versus open boundary conditions

As discussed in the main text, the choice of OBC causes the emergence of disjoint Krylov subspaces $\mathcal{K}_{du}$. This fact can be exemplified by contrasting the entanglement entropies $S_{|n\rangle}$ of eigenstates of $\mathcal{H}_\nu$ for PBC and OBC. In the case of PBC [Fig. S1 (a)], we find that $S_{|n\rangle}$ behaves as one would expect for a nonintegrable and thermalizing system, i.e., $S_{|n\rangle}$ takes on extensive values in the center of the spectrum which are similar to those of random states, while the entanglement towards the edges of the spectrum is lower. Interestingly, a degenerate set of zero-energy eigenstates, well separated from the band of thermal states, can be identified as well. Thus, similar to the states $|\mathcal{S}_\nu\rangle$ discussed in the main text, scarred eigenstates also exist for PBC. Specifically, since lattice momentum κ is a good quantum number for PBC, these quantum scars then belong to sectors with different κ [S1]. In contrast, in the case of OBC [Fig. S1 (b)], the distribution of $S_{|n\rangle}$ is rather broad due to the disjoint $\mathcal{K}_{du}$. Note that the data in Fig. S1 (b) was already shown in Fig. 2 (a) of the main text. In Fig. S1 (b) we now additionally highlight the comparatively low entanglement of the quantum many-body scars $|\mathcal{S}_\nu\rangle$ belonging to different $\mathcal{K}_{du}$.

Level-spacing distribution

As the Hilbert space splits into Krylov spaces with a fixed number of unpaired spins N_d, N_u, chaos and thermalization has to be studied within each such subspace. A common diagnostic is the distribution $P(\Delta)$ of adjacent level spacings $\Delta_n = E_{n+1} - E_n$. In Fig. S2 (a), $P(\Delta)$ is shown for a fixed system size $L = 12$ in the largest Krylov subspace with $N_d = N_u = 1$. For all values of ν considered here, we find that $P(\Delta)$ accurately follows a Wigner-Dyson distribution, indicating the onset of quantum chaos [S2].

To study the statistics of energy levels for a wider range of ν and N_d, Fig. S2 (b) shows the mean ratio $\langle r \rangle$ of adjacent level spacings [S3],

$$\langle r \rangle = \frac{1}{N} \sum_n \frac{\min\{\Delta_n, \Delta_{n+1}\}}{\max\{\Delta_n, \Delta_{n+1}\}} \ , \tag{S1}$$

where the averaging is here performed over roughly $N = 2\mathcal{D}_{du}/3$ of the eigenstates around the center of each Krylov space. For chaotic models, one expects $\langle r \rangle$ to be similar to the ratio of a random matrix, e.g., drawn from the Gaussian orthogonal ensemble (GOE), $\langle r \rangle_{\mathrm{GOE}} \approx 0.53$. In contrast, for integrable or many-body localized models, the level spacing is Poissonian with $\langle r \rangle \approx 0.39$ [S2].

As shown in Fig. S2 (b), we find $\langle r \rangle \approx 0.53$ for almost the whole range of $\nu \leq 2$ considered here (the agreement is slightly better for Krylov spaces with a larger dimension $\mathcal{D}_{du}$). Only if ν becomes too small, deviations from the random-matrix value appear, which can be explained by $\mathcal{H}_\nu$ becoming entirely diagonal for $\nu \to 0$ with a highly degenerate spectrum. We have spot-checked that $\langle r \rangle \approx 0.53$ also holds for the largest Krylov spaces in sectors with $S^z \neq 0$ (not shown here). Since the dimensions $\mathcal{D}_{du}$ of Krylov spaces with large N_d, N_u become too small to obtain good statistics, we refrain from searching in more detail for $\mathcal{K}_{du}$ that might exhibit Poissonian statistics. We note, however, that subspaces with large N_d, N_u can indeed exhibit peculiar behavior. For instance, the subspace with $N_d = N_u = 4$, depicted in Fig. 2 (a) of the main text, features a degenerate set of zero-energy eigenstates in addition to the exact state $|\mathcal{S}_\nu\rangle$.
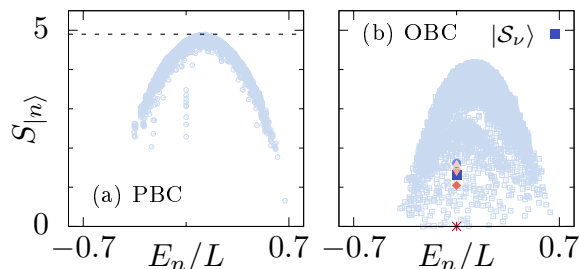

FIG. S1. Eigenstate entanglement for (a) PBC and (b) OBC in the $S^z = 0$ sector. The horizontal dashed line in (a) indicates the entanglement of a random state. In (b), the exact quantum scars $|\mathcal{S}_\nu\rangle$ belonging to different Krylov subspaces are indicated by symbols. We have $L = 10$, $c_1 = c_3 = 1$, and $c_2 = -1$ in all cases.
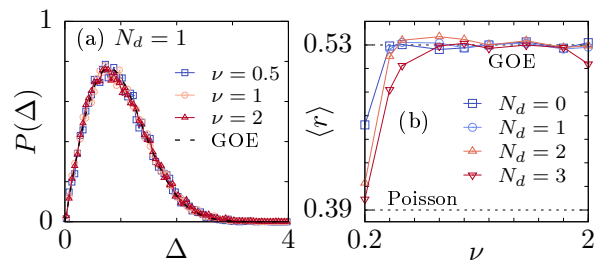

FIG. S2. (a) Distribution $P(\Delta)$ of energy gaps in the Krylov space with $N_d = N_u = 1$ for $\nu = 0.5, 1, 2$. The dashed curve indicates the quantum-chaotic Wigner-Dyson distribution. Note that the correct extraction of $P(\Delta)$ requires an unfolding of the spectrum. (b) $\langle r \rangle$ versus ν for Krylov spaces with different $N_d = N_u$. The dashed horizontal lines indicates the GOE and the Poissonian value respectively. We have $L = 12$, $c_1 = c_3 = 1$, and $c_2 = -1$ in all cases.
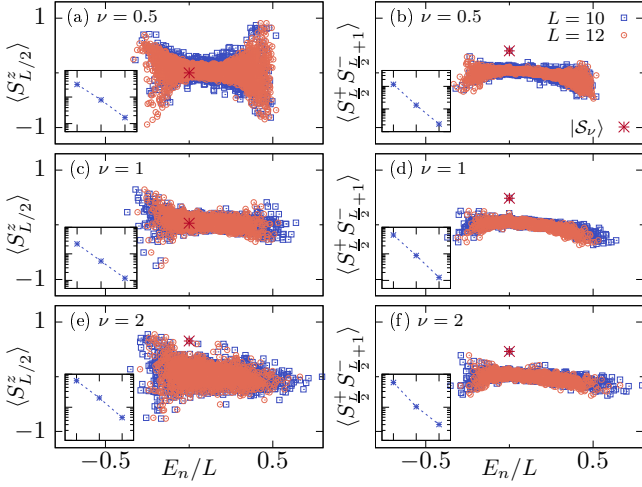
FIG. S3. Eigenstate expectation values $\langle \cdot \rangle = \langle n | \cdot | n \rangle$ versus energy density for the two operators $S_{L/2}^z$ (left column) and $S_{L/2}^+ S_{L/2+1}^-$ (right column). Data is shown for $\nu = 0.5, 1, 2$ (top to bottom) and two different system sizes $L = 10, 12$ in the Krylov space with $N_d = N_u = 0$. The expectation values with respect to the exact scar eigenstate $|\mathcal{S}_\nu\rangle$ are highlighted by an asterisk. The insets show the variances of the $\langle n | \cdot | n \rangle$, evaluated within a narrow energy window in the center of the spectrum (excluding the scar $|\mathcal{S}_\nu\rangle$), versus system sizes $L = 8, 10, 12$. For all cases considered, the variances decrease approximately exponentially with L.

Validity of eigenstate thermalization hypothesis (ETH)

According to the ETH, the diagonal matrix elements of physical operators written in the eigenbasis of chaotic Hamiltonians should be a smooth function of energy [S2]. In Fig. S3, we test the ETH for two local operators defined in the center of the chain,

$$\mathcal{O}_1 = S_{L/2}^z, \quad \mathcal{O}_2 = S_{L/2}^+ S_{L/2+1}^- . \quad \text{(S2)}$$

Focusing on the Krylov space with $N_d = N_u = 0$, Figs. S3 (a)-(f) show the "cloud" of diagonal elements $\langle n | \mathcal{O}_{1/2} | n \rangle$ for three different values of the deformation parameter $\nu = 0.5, 1, 2$, and two different system sizes $L = 10, 12$. Generally, the $\langle n | \mathcal{O}_{1/2} | n \rangle$ behave consistent with other known examples in the literature [S2], i.e., the distributions are relatively broad at the edges of the spectrum, while they narrow down in the center. Especially for $\mathcal{O}_1$, we find that the distribution of the $\langle n | \mathcal{O}_1 | n \rangle$ notably depends on ν, with a broader distribution for $\nu = 2$ and a narrower distribution for $\nu = 0.5$. While it is hard to see from the bare distributions in Fig. S3, we have checked that the variances of the $\langle n | \mathcal{O}_{1/2} | n \rangle$ actually decrease approximately exponentially with increasing L for all ν (see insets in Fig. S3 and caption for description). Thus, we expect that in the thermodynamic limit $L \to \infty$, the overwhelming majority of eigenstates of $\mathcal{H}_\nu$ follows the ETH.
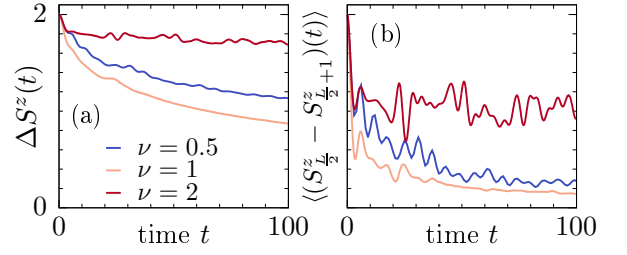

FIG. S4. (a) Magnetization difference $\Delta S^z(t)$ [Eq. (S3)] between the two halves of the chain. (b) Magnetization difference $\langle S_{L/2}^z(t) \rangle - \langle S_{L/2+1}^z(t) \rangle$ between the two central lattice sites. Note that the curve for $\nu = 2$ in (b) is very similar to the Loschmidt echo $\mathcal{L}(t)$ in Fig. 5. We have $L = 16$ in all cases.

In Fig. S3, we additionally highlight the expectation value $\langle S_\nu | \mathcal{O}_{1/2} | S_\nu \rangle$ with respect to the exact eigenstate $|S_\nu\rangle$. In the case of $\mathcal{O}_1$, we find $\langle S_\nu | \mathcal{O}_1 | S_\nu \rangle \approx 0$ for $\nu = 0.5, 1$ such that $|S_\nu\rangle$ is indistinguishable from the thermal eigenstates in its vicinity. Interestingly, for $\nu = 2$ [Fig. S3 (e)], $|S_\nu\rangle$ yields a nonzero value of $\mathcal{O}_1$, which also reflects itself in the quench dynamics of the domain-wall state at $\nu = 2$ (Fig. 5 of main text). In contrast, in the case of $\mathcal{O}_2$ [Figs. S3 (b),(d),(f)], we find $\langle n | \mathcal{O}_2 | n \rangle \approx 0$ for most $|n\rangle$, while the exact state $|S_\nu\rangle$ yields a nonzero expectation value which is a clear outlier well separated from the bulk of the thermal states, demonstrating the embedding of a quantum many-body scar into the spectrum of $\mathcal{H}_\nu$.

Additional data on domain-wall melting

Let us present additional data on the melting of domain-wall initial states considered in Fig. 5 of the main text. Figure S4 (a) shows the magnetization difference $\Delta S^z(t)$ between the two halves of the system for $\nu = 0.5, 1, 2$,

$$\Delta S^z(t) = \frac{2}{L} \sum_{\ell=1}^{L/2} \left(\langle S_\ell^z(t) \rangle - \langle S_{L/2+\ell}^z(t) \rangle \right) . \quad \text{(S3)}$$

Consistent with the earlier data shown in Figs. 5 (c) and (d), $\Delta S^z(t)$ continues to decay for $\nu = 0.5, 1$ even at long times $t = 100$, while the dynamics is very slow for $\nu = 2$. Moreover, Fig. S4 (b) shows the magnetization difference only between the two central sites of the lattice. We find that $\langle S_{L/2}^z(t) \rangle - \langle S_{L/2+1}^z(t) \rangle$ decays almost to zero for $\nu = 0.5, 1$ (i.e., the spin profile becomes smooth in the center), whereas a finite magnetization jump remains in the case of $\nu = 2$. In this context, it is also instructive to compare the curve of $\langle S_{L/2}^z(t) \rangle - \langle S_{L/2+1}^z(t) \rangle$ for $\nu = 2$ in Fig. S4 (b) to the decay of the Loschmidt echo $\mathcal{L}(t)$ in Fig. 5 (a) of the main text. Quite remarkably, one finds that the two curves are very similar to each other, even
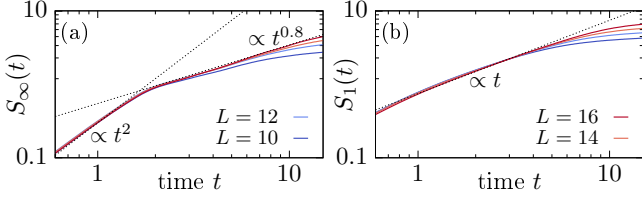
FIG. S5. (a) $S_\infty(t)$ and (b) $S_1(t)$ for chains with PBC and different L, obtained by averaging over multiple product states in the $S^z = 0$ sector. Power laws are shown for comparison.

FIG. S6. [(a),(b)] $\mathcal{L}(t) = |\langle\psi(t)|\psi\rangle|^2$ and entanglement $S_1(t) = \text{Tr}[\rho_A(t)\ln\rho_A(t)]$ for the initial state $|udud\cdots\rangle$. [(c)-(e)] Color plot of $\langle\psi(t)| S_\ell |\psi(t)\rangle$ for $\nu = 0.5, 1, 2$. We have $L = 14$, $c_1 = c_3 = 1$, and $c_2 = -1$ in all cases.

on the level of individual (finite-size) fluctuations. This observation is in good agreement with a typicality-based framework developed in [S4], which predicts that the dynamics of observables is closely related to $\mathcal{L}(t)$ in situations where one eigenstate (here the exact state $|\mathcal{S}_\nu\rangle$) is macroscopically populated.

Entanglement growth

To complement the analysis of anomalous hydrodynamics from the main text, we here study the Rényi entropies $S_\alpha(t) = \ln\text{Tr}[\rho_A^\alpha]/(1-\alpha)$, $\rho_A = \text{Tr}_B |\psi(t)\rangle\langle\psi(t)|$, which were argued to grow subballistically for $\alpha > 1$ [S5, S6]. Focusing on the extremal case $S_\infty(t) = -\ln\lambda_{\max}$, where $\lambda_{\max}$ is the largest eigenvalue of ρ_A, $\mathcal{H}_\nu$ indeed yields a rather unusual build-up of entanglement with $S_\infty(t) \propto t^2$ at short times (similar to strongly coupled holographic systems [S7]) and $S_\infty(t) \propto t^{0.8}$ at larger t, see Fig. S5 (a). While $S_\infty(t)$ thus neither grows diffusive [S5, S6], nor agrees with the conjecture $S_{\alpha>1}(t) \propto t^{1/z}$ [S5, S8, S9], we note that models with spin $S \geq 1$ might exhibit subleties [S8, S9]. In this context, let us stress that a numerical analysis is complicated due to finite-size effects such that potential changes in the growth rate at later times cannot be accessed. In contrast to $S_\infty(t)$, the von Neumann entropy $S_1(t) \propto t$ [Fig. S5 (b)] scales linearly as expected.

Quench dynamics for another initial state

In the main text, we have exemplified the impact of the scar $|\mathcal{S}_\nu\rangle$ on the dynamics by considering a domain-wall initial state $|u\cdots ud\cdots d\rangle$, which can be tuned between a localized and a delocalized regime depending on the choice of ν. Let us here present additional data for another initial state, namely a Néel-like state $|\psi\rangle = |udud\cdots\rangle$ which likewise belogs to the Krylov space $\mathcal{K}_{00}$. In contrast to the domain wall, which maximizes the area $\mathcal{A}$, the Néel state yields a much smaller $\mathcal{A}$. As a consequence, in costrast to Fig. 5 in the main text, the overlap between $|\mathcal{S}_\nu\rangle$ and $|\psi\rangle$ is now enhanced for $\nu < 1$, leading to slower thermalization for $\nu < 1$. This
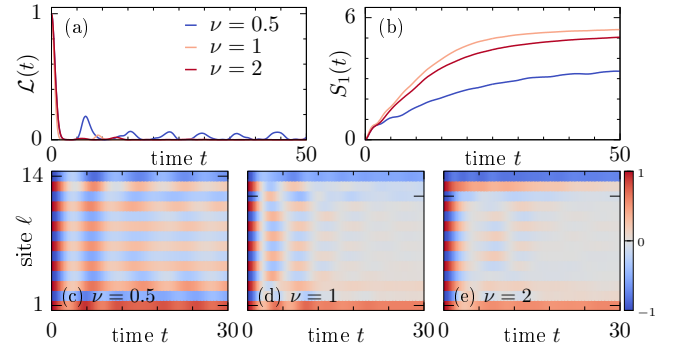
is demonstrated in Fig. S6, where $\mathcal{L}(t) = |\langle\psi(t)|\psi\rangle|^2$ quickly decays for $\nu = 1, 2$, while revivals are present for $\nu = 0.5$ [Fig. S6 (a)], accompanied by a faster growth of entanglement for $\nu \geq 1$ [Fig. S6 (b)]. Likewise, the $\cdots ud\cdots$ pattern remains more stable for $\nu = 0.5$ [Fig. S6 (c)], while fast bulk thermalization occurs for $\nu = 1, 2$ [Figs. S6 (d) and (e)].

Construction of $|\mathcal{S}_\nu\rangle$

According to Eq. (3) in the main text, the exact eigenstate $|\mathcal{S}_\nu\rangle$ is given by the area-weighted superposition of all basis states in a given Krylov space. While we refer to Refs. [S10–S12] for details on $|\mathcal{S}_\nu\rangle$ indeed being an eigenstate of $\mathcal{H}_\nu$, let us here derive the second part of Eq. (3), i.e., relating the area of a given spin configuration to its dipole moment (see also [S13]). To this end, we introduce the height h_ℓ of a spin configuration at position ℓ,

$$h_\ell = \sum_{l=1}^{\ell} S_l^z \ , \tag{S4}$$

where we define $h_0 = 0$. Using this, the area $\mathcal{A}_k = \langle k| \mathcal{A} |k\rangle$ of a spin configuration follows as,

$$\mathcal{A} = \sum_{\ell=1}^{L}(h_\ell + h_{\ell-1})/2 \tag{S5}$$

$$= \sum_{\ell=1}^{L}\left(\sum_{l=1}^{\ell} S_l^z + \sum_{l=1}^{\ell-1} S_l^z\right)/2 \tag{S6}$$

$$= S^z/2 + \sum_{\ell=1}^{L}\sum_{l=1}^{\ell-1} S_l^z \tag{S7}$$

$$= S^z/2 + \sum_{\ell=1}^{L}(L-\ell)S_\ell^z \tag{S8}$$

$$= (2L+1)S^z/2 - \mathcal{P} \ , \tag{S9}$$

where $S^z = \sum_{\ell=1}^{L} S_\ell^z$ and $\mathcal{P}$ is the dipole operator. Since the $|\mathcal{S}_\nu\rangle$ are defined within a sector with fixed magnetization S^z, $\langle k| S^z |k\rangle$ will be independent of the specific basis state $|k\rangle$ such that the first term on the right hand side of Eq. (S9) can be dropped. It then follows that,

$$|\mathcal{S}_\nu\rangle = \frac{1}{\sqrt{M'_\nu}} \sum_k \nu^{\mathcal{A}_k} |k\rangle = \frac{1}{\sqrt{M_\nu}} \sum_k \nu^{-\mathcal{P}_k} |k\rangle \ . \quad (S10)$$

where $M'_\nu = \sum_k \nu^{2\mathcal{A}_k}$ and $M_\nu = \sum_k \nu^{-2\mathcal{P}_k}$.

Dynamical quantum typicality

The correlation function $C(r,t)$ in Eq. (4) can be efficiently calculated by means of the concept of dynamical quantum typicality (DQT) [S14, S15]. To this end, let $|\mathcal{R}\rangle = \sum_k c_k |k\rangle$ be a Haar-random state drawn from the full Hilbert space, i.e., in practice the sum runs over the 3^L computational basis states $|k\rangle$ and the real and imaginary parts of the complex coefficients c_k are drawn from a Gaussian distribution with zero mean. We assume $\sum_k |c_k|^2 = 1$. According to DQT, $C(r,t)$ can then be approximated as (see also [S16, S17] for detailed derivations),

$$C(r,t) = \langle\mathcal{R}_\ell(t)| S_{\ell+r}^z |\mathcal{R}_\ell(t)\rangle + \varepsilon(|\mathcal{R}\rangle) \ , \quad (S11)$$

where $|\mathcal{R}_\ell\rangle = \sqrt{S_\ell^z + 1} |\mathcal{R}\rangle$ and $|\mathcal{R}_\ell(t)\rangle = e^{-i\mathcal{H}t} |\mathcal{R}_\ell\rangle$. Importantly, the statistical error of the approximation in Eq. (S11) scales as $\varepsilon(|\mathcal{R}\rangle) \propto 1/\sqrt{3^L}$ [S14, S15], and can therefore be neglected already for intermediate system sizes. Thus, the correlation function $C(r,t)$ is faithfully approximated by the expectation value of $S_{\ell+r}^z$ within the random state $|\mathcal{R}_\ell(t)\rangle$. Since the time evolution of $|\mathcal{R}_\ell(t)\rangle$ can be evaluated efficiently by standard sparse-matrix techniques [S18], $C(r,t)$ can be simulated for system sizes beyond the range of ED.

Details on stochastic cellular automaton dynamics

In order to substantiate our direct simulations of the transport properties of the Motzkin chain $\mathcal{H}_\nu$ (i.e., as obtained under full quantum evolution on system sizes $L \leq 18$), we have constructed a stochastic cellular automaton (CA) circuit (or Markov chain) [S19–S23]. The CA circuit is constructed in such a way, that it mimics the terms appearing in $\mathcal{H}_\nu$ [Fig. 1 (a)]. It is composed of two-site updates $\mathcal{U}$ which map product states from the 3^L-dimensional computational basis to other product states (e.g., $\mathcal{U} |0du00d\cdots\rangle \to |d00u0d\cdots\rangle$), i.e., no entanglement is created when the initial state of the circuit is itself a member of the computational basis. As a consequence, classical simulations of large system sizes and long time scales are possible [S19–S23]. Note, however, that the induced operator dynamics in the Heisenberg

picture, $S_\ell^z \to \mathcal{U}^\dagger S_\ell^z \mathcal{U}$, can be more complicated and can share features of a more generic (chaotic) Hamiltonian evolution [S19].

In Fig. 3 of the main text, a single exemplary time step of the stochastic automaton evolution is illustrated. Starting with an arbitrary configuration in the computational basis, we consider three different types of local updates, named D, U, and V [in accordance with the projectors in Eq. (1)]. Given a configuration of the two neighboring spins, the appropriate local update is chosen, where D acts as $|0d\rangle \leftrightarrow |d0\rangle$, U acts as $|0u\rangle \leftrightarrow |u0\rangle$, and V acts as $|00\rangle \leftrightarrow |ud\rangle$, i.e., these updates correspond to the off-diagonal terms of $\mathcal{H}_\nu$. However, with a probability of $1/2$ (hence *stochastic* circuit), the updates D, U, or V are replaced by $\bar{D}$, $\bar{U}$, $\bar{V}$, which act as the identity, such that the local configuration remains unchanged (see gray gates in Fig. 3), i.e., these cases correspond to the diagonal terms of $\mathcal{H}_\nu$. Likewise, if the two-site configuration is given by $|dd\rangle$, $|uu\rangle$, or $|du\rangle$, no local update is performed as $\mathcal{H}_\nu$ does not contain corresponding terms (such a case is not shown in Fig. 3). A full time step in the circuit then consists of two layers of local two-site updates, where the local unitary transformations first act on all even bonds and subsequently on all odd bonds. Moreover, the infinite-temperature spin-spin correlation function $C(r,t)$ in Eq. (4) is obtained by averaging the classical quantity $S_{\ell+r}^z(t) S_\ell^z(0)$ over sufficiently many initial spin configurations.

Derivation of spin-current operator

Let us derive the expression for the spin-current operator of the Motzkin chain. Inspecting the Hamiltonian in Eq. (1), the relevant contributions to spin transport are given by the off-diagonal terms $c_1\nu(-|0d\rangle\langle d0| - |d0\rangle\langle 0d|)/(1+\nu^2)$, $c_2\nu(-|0u\rangle\langle u0| - |u0\rangle\langle 0u|)/(1+\nu^2)$, and $c_3\nu(-|00\rangle\langle ud| - |ud\rangle\langle 00|)/(1+\nu^2)$, while the diagonal terms can be ignored. It is further helpful to rewrite the above expressions in terms of spin-1 operators. For example, one finds [S24],

$$|0d\rangle\langle d0| = S_1^+ S_1^z S_2^z S_2^- \ , \quad (S12)$$

and the other off-diagonal terms have similar representations that we here omit for brevity. The spin current now follows from the lattice continuity equation $\frac{d}{dt} S_\ell^z = i[\mathcal{H}_\nu, S_\ell^z] = j_{\ell-1} - j_\ell$ [S25]. Note that the commutator is non-vanishing only for the local terms of $\mathcal{H}_\nu$ acting on sites $\ell-1, \ell$ and $\ell, \ell+1$. Using the identity $[S_\ell^\pm, S_{\ell'}^z] = \mp S_\ell^\pm \delta_{\ell\ell'}$ and carrying out some straightforward manipulations, one finds that $j = \sum_\ell j_\ell$ with,

$$\begin{aligned} j_\ell = \frac{i\nu}{1+\nu^2} \big[&(c_3 S_\ell^z S_\ell^+ - c_1 S_\ell^+ S_\ell^z) S_{\ell+1}^z S_{\ell+1}^- \quad (S13) \\ &+ S_\ell^- S_\ell^z (c_2 S_{\ell+1}^z S_{\ell+1}^+ - c_3 S_{\ell+1}^+ S_{\ell+1}^z) \\ &+ S_\ell^z (c_1 S_\ell^- S_{\ell+1}^+ - c_2 S_\ell^+ S_{\ell+1}^-) S_{\ell+1}^z \big] \ . \end{aligned}$$

At $\nu = c_i = 1$, the local terms in Eq. (S13) can be substantially simplified and take on the form,

$$j_\ell = \frac{i}{2} \big[S_\ell^+ S_{\ell+1}^z S_{\ell+1}^- + S_\ell^- S_\ell^z S_{\ell+1}^+ \tag{S14}$$
$$+ S_\ell^z (S_\ell^- S_{\ell+1}^+ - S_\ell^+ S_{\ell+1}^-) S_{\ell+1}^z \big] \ ,$$

where we again exploited the commutator relations of $S_\ell^\pm$ and S_ℓ^z. It is insightful to contrast Eq. (S14) with the spin current of a more common spin-1 model, e.g, the Heisenberg chain, $\mathcal{H}_{\mathrm{Heis}} = \sum_\ell \mathbf{S}_\ell \cdot \mathbf{S}_{\ell+1}$, for which the current has the well-known form $j_{\mathrm{Heis}} = \frac{i}{2} \sum_\ell (S_\ell^+ S_{\ell+1}^- - S_\ell^- S_{\ell+1}^+)$ [S25]. Comparing j_{Heis} to Eq. (S14), j is essentially a dressed version of j_{Heis}, which formalizes that some configurations do not contribute to the transport of spin in the Motzkin chain.

* j.richter@ucl.ac.uk

[S1] O. Salberger and V. Korepin, Rev. Math. Phys. **29**, 1750031 (2017).

[S2] L. D'Alessio, Y. Kafri, A. Polkovnikov, and M. Rigol, Adv. Phys. **65**, 239 (2016).

[S3] V. Oganesyan and D. A. Huse, Phys. Rev. B **75**, 155111 (2007).

[S4] P. Reimann, B. N. Balz, J. Richter, and R. Steinigeweg, Phys. Rev. B **101**, 094302 (2020).

[S5] T. Rakovszky, F. Pollmann, and C. W. von Keyserlingk, Phys. Rev. Lett. **122**, 250602 (2019).

[S6] Y. Huang, IOP SciNotes **1**, 035205 (2020)

[S7] H. Liu and S. J. Suh, Phys. Rev. Lett. **112**, 011601 (2014).

[S8] M. Žnidarič, Commun. Phys. **3**, 100 (2020).

[S9] T. Rakovszky, F. Pollmann, and C. von Keyserlingk, Commun. Phys. **4**, 91 (2021).

[S10] S. Bravyi, L. Caha, R. Movassagh, D. Nagaj, and P. W. Shor, Phys. Rev. Lett. **109**, 207202 (2012).

[S11] Z. Zhang, A. Ahmadain, and I. Klich, PNAS **114**, 5142 (2017).

[S12] R. Movassagh and P. W. Shor, PNAS **113**, 13278 (2016).

[S13] C. Langlett and S. Xu, Phys. Rev. B **103**, L220304 (2021).

[S14] F. Jin, D. Willsch, M. Willsch, H. Lagemann, K. Michielsen, and H. De Raedt, J. Phys. Soc. Jpn. **90**, 012001 (2021).

[S15] T. Heitmann, J. Richter, D. Schubert, and R. Steinigeweg, Z. Naturforsch. A **75**, 421 (2020).

[S16] J. Richter and A. Pal, Phys. Rev. Lett. **126**, 230501 (2021).

[S17] C. Chiaracane, F. Pietracaprina, A. Purkayastha, and J. Goold, Phys. Rev. B **103**, 184205 (2021).

[S18] H. Fehske, J. Schleede, G. Schubert, G. Wellein, V. S. Filinov and A. R. Bishop, Phys. Lett. A **373**, 2182 (2009).

[S19] J. Iaconis, S. Vijay, and R. Nandkishore, Phys. Rev. B **100**, 214301 (2019).

[S20] J. Feldmeier, P. Sala, G. De Tomasi, F. Pollmann, and M. Knap, Phys. Rev. Lett. **125**, 245303 (2020).

[S21] A. Morningstar, V. Khemani, and D. A. Huse, Phys. Rev. B **101**, 214205 (2020).

[S22] M. Medenjak, K. Klobas, and T. Prosen, Phys. Rev. Lett. **119**, 110603 (2017).

[S23] S. Gopalakrishnan and B. Zakirov, Quantum Sci. Technol. **3**, 033004 (2018).

[S24] X. Chen, E. Fradkin, and W. Witczak-Krempa, J. Phys. A: Math. Theor. **50**, 464002 (2017).

[S25] B. Bertini, F. Heidrich-Meisner, C. Karrasch, T. Prosen, R. Steinigeweg, and M. Žnidarič, Rev. Mod. Phys. **93**, 025003 (2021).